



Article

First-Principle Investigations on the Electronic and Transport Properties of $\text{PbBi}_2\text{Te}_2\text{X}_2$ ($\text{X} = \text{S}/\text{Se}/\text{Te}$) Monolayers

Weiliang Ma ^{1,2} , Jing Tian ^{1,2} , Pascal Boulet ² and Marie-Christine Record ^{1,*}

¹ IM2NP, CNRS, Faculty of Sciences, Aix-Marseille University, 13013 Marseille, France; weiliang.ma@etu.univ-amu.fr (W.M.); jing.tian@etu.univ-amu.fr (J.T.)

² MADIREL, CNRS, Faculty of Sciences, Aix-Marseille University, 13013 Marseille, France; pascal.boulet@univ-amu.fr

* Correspondence: m-c.record@univ-amu.fr

Abstract: This paper reports first-principles calculations on $\text{PbBi}_2\text{Te}_2\text{S}_2$, $\text{PbBi}_2\text{Te}_2\text{Se}_2$ and PbBi_2Te_4 monolayers. The strain effects on their electronic and thermoelectric properties as well as on their stability have been investigated. Without strain, the PbBi_2Te_4 monolayer exhibits highest Seebeck coefficient with a maximum value of $671 \mu\text{V}/\text{K}$. Under tensile strain the highest power factor are $12.38 \times 10^{11} \text{ W m}^{-1}\text{K}^{-2}\text{s}^{-1}$, $10.74 \times 10^{11} \text{ W m}^{-1}\text{K}^{-2}\text{s}^{-1}$ and $6.51 \times 10^{11} \text{ W m}^{-1}\text{K}^{-2}\text{s}^{-1}$ for $\text{PbBi}_2\text{Te}_2\text{S}_2$, $\text{PbBi}_2\text{Te}_2\text{Se}_2$ and PbBi_2Te_4 at 3%, 2% and 1% tensile strains, respectively. These values are 85.9%, 55.0% and 3.3% larger than those of the unstrained structures.

Keywords: 2D materials; chalcogenides; thermoelectric properties; strain effects; DFT



Citation: Ma, W.; Tian, J.; Boulet, P.; Record, M.-C. First-Principle Investigations on the Electronic and Transport Properties of $\text{PbBi}_2\text{Te}_2\text{X}_2$ ($\text{X} = \text{S}/\text{Se}/\text{Te}$) Monolayers. *Nanomaterials* **2021**, *11*, 2979. <https://doi.org/10.3390/nano11112979>

Academic Editor: Nikolai V. Tkachenko

Received: 18 September 2021
Accepted: 30 October 2021
Published: 5 November 2021

Publisher's Note: MDPI stays neutral with regard to jurisdictional claims in published maps and institutional affiliations.



Copyright: © 2021 by the authors. Licensee MDPI, Basel, Switzerland. This article is an open access article distributed under the terms and conditions of the Creative Commons Attribution (CC BY) license (<https://creativecommons.org/licenses/by/4.0/>).

1. Introduction

Thermoelectric (TE) materials that enable direct electrothermal energy conversion can have important applications in power generation [1,2], the recovery of waste heat, and on-chip cooling [3,4] and can thus provide a new route for green, clean energy to tackle the global energy crisis. However the application of TE devices has been limited by the low efficiency of their constitutive materials [5,6]. The energy conversion efficiency of TE materials is determined by the figure of merit $zT = S^2\sigma T / (\kappa_e + \kappa_l)$, where S is the Seebeck coefficient, σ is the electrical conductivity, κ_e and κ_l are the electronic and lattice thermal conductivities, respectively, and T is the temperature. As a consequence, an improvement of the TE performance requires increasing the power factor ($PF = S^2\sigma$) and/or reducing the total thermal conductivity. Several effective strategies such as the optimization of the carriers density, the convergence of the electronic bands [7,8], and the introduction of resonant states [9,10] have been proposed to enhance PF . For instance, Diznab [8] recently boosted the PF of Bi_2Te_3 monolayer by 43.6% via valence band convergence obtained through Se substitution for Te. Besides, the existence of a resonant level in Tl-doped PbTe and in $\text{Tl}_{0.02}\text{Pb}_{0.98}\text{TeSi}_{0.02}\text{Na}_{0.02}$ boosts the Seebeck coefficient, allowing zT for reaching a value of 1.5 [10] and 1.7 [11], respectively. Apart from band engineering, zT can also be improved by the so-called phonon engineering through reducing the material's dimensionality or generating superlattices. This strategy has proved efficient in n-type $\text{Bi}_2\text{Te}_{2.7}\text{Se}_{0.3}$ nanowires with a 13% zT improvement [12].

Among many TE materials systems proposed in the past decades, complex layered chalcogenides are potential candidates for TE applications due to their low κ_l . Based on the methods mentioned above, the zT value has been pushed up to 2.2 for phase-separated $\text{PbTe}_{0.7}\text{S}_{0.3}$ [13], 1.86 for $\text{Bi}_{0.5}\text{Sb}_{1.5}\text{Te}_3$ [14] and 2.5 for PbTe -8% SrTe [15]. Furthermore, experimental measurements and theoretical calculations reveal that monolayer structures are promising for future TE applications [12,16,17], since they benefit from the combination of two complementary approaches, namely the electronic band engineering and the phonon one. As reported in literature for MoS_2 , Bi_2Te_3 and Bi_2Se_3 [18–20], monolayer or few-layer

nanosheets can be experimentally obtained by exfoliation from the bulk, or synthesized by solution-phase method as with PbBi_2Te_4 and $\text{Pb}_2\text{Bi}_2\text{Te}_5$ [21]. Due to their layered structures involving van der Waal interactions, these latter compounds present additional interest for future TE application, namely an intrinsically low thermal conductivity and the possibility to obtain few-layer thick nanosheets by exfoliation from the bulk.

The bulk compounds in the $n(\text{PbTe})\text{-}m(\text{Bi}_2\text{Te}_3)$ system bearing a layered structure are the following: Bi_2Te_3 with a quintuple layers structure and sequence -Te-Bi-Te-Bi-Te-, PbBi_2Te_4 with a septenary layers structure and sequence -Te-Bi-Te-Pb-Te-Bi-Te-, and $\text{Pb}_2\text{Bi}_2\text{Te}_5$ with an ennead layers structure and sequence -Te-Bi-Te-Pb-Te-Pb-Te-Bi-Te-. Among them, topologically protected surface states have been found in Bi_2Te_3 thin film [22], $\text{PbBi}_2\text{Te}_2\text{Se}_2$ monolayer [23] and PbBi_2Te_4 bilayer [24], leading to the intrinsic convergence of multivalley bands, which is the most interesting for improving TE properties. Benefiting from band convergence and quantum confinement, the single quintuple tetradymites family of Bi_2X_3 ($\text{X} = \text{S}, \text{Se}, \text{Te}$) exhibits high zT values of 1.4–2.4 [8,25,26] and have been widely investigated to date. Hence, in this study, we have focused our investigation on the PbBi_2Te_4 nanosheet and $\text{PbBi}_2\text{Te}_2\text{Se}_2$ and $\text{PbBi}_2\text{Te}_2\text{S}_2$ ones, which have been obtained by substituting Se and S for two Te atoms in PbBi_2Te_4 . Using DFT calculations, we have determined the stability, the electronic structure, the TE properties, and the thermal conductivity of these nanosheets. We have also explored the effect of bi-axial strains on their properties.

2. Materials and Methods

DFT calculations have been performed using the all-electron FP-LAPW approach with local orbital method as implemented in WIEN2K [27]. To obtain a good convergence, the plane wave cut-off criterium $R_{mt}K_{max}$ was set to 9.0, and the k-meshes used to sample the Brillouin zone have been set to $12 \times 12 \times 1$ for structural optimization and $16 \times 16 \times 1$ for self-consistent energy calculations. The total energy and atomic forces convergence thresholds have been defined as 0.068 meV and $0.257 \text{ meV}/\text{\AA}$ for the three compounds $\text{PbBi}_2\text{Te}_2\text{S}_2$, $\text{PbBi}_2\text{Te}_2\text{Se}_2$ and PbBi_2Te_4 . The energy separation between the core and valence electrons has been fixed at -5.0 Ry . The electronic transport properties, namely S , κ_e , and σ have been calculated by solving the Boltzmann semi-classical transport equation as implemented in BoltzTraP2 [28]. The implementation of BoltzTraP2 is based on the use of full band structure in the Brillouin zone (BZ). Herein, the BZ has been sampled using a dense k-mesh of $64 \times 4 \times 8$, and we have checked that the interpolation of the band structure performed by BoltzTraP2 properly reproduced the DFT band structure.

Second and third order anharmonic interatomic force constants (IFCs) have been calculated by means of the DFPT method by using the QUANTUM-ESPRESSO package [29] together with the Phonopy and Phono3py programs [30]. A supercell of $5 \times 5 \times 1$ with a k-mesh of $4 \times 4 \times 2$ and a supercell of $4 \times 4 \times 1$ with a Γ k-point calculation have been considered for second and third order IFCs evaluations, respectively. The calculation is carried out by using the projector augmented-wave pseudopotential method with a plane-wave energy cutoff of 70 Ry (952 eV) and a total force threshold of 10^{-4} Ry/bohr . In subsequent post-processing calculations, phonon lifetimes have been sampled using a $43 \times 43 \times 7$ mesh. The lattice thermal conductivity has been calculated by using both a full solution of the linearized phonon Boltzmann equation (LBTE) method as introduced in ref. [31] and the relaxation time approximation (RTA) method. Within the RTA method, the lattice thermal conductivity tensor $\kappa_l^{\alpha\beta}$ is expressed as

$$\kappa_l^{\alpha\beta} = \frac{1}{NV_0} \sum_{\lambda} C_{\lambda} v_{\lambda}^{\alpha} v_{\lambda}^{\beta} \tau_{\lambda} \quad ,$$

where N is the number of q-points, V_0 is the unit cell volume, v_{λ} is the group velocity indexed with the Cartesian coordinates α and β , and τ_{λ} is the phonon scattering time for the specific phonon mode λ . The heat capacity for the specific phonon mode with

frequency ω_λ is $C_\lambda = k_B \left(\frac{\hbar^2 \omega_\lambda}{k_B T} \right)^2 n_\lambda^0 (n_\lambda^0 + 1)$, where n_λ^0 is the Bose-Einstein distribution function. The spectral representation of the dynamical thermal conductivity obtained from the LBTE method is $\kappa_l = \int d\omega' \frac{\rho(\omega')}{\omega' - i\omega}$, where $\rho(\omega')$ is the spectral density. Furthermore, because the lattice thermal conductivity is an intensive property for bulk materials, that of two-dimensional material should be normalized by multiplying by L_z/d , where L_z is the lattice parameter c and d is the thickness of the nanosheet.

3. Results

3.1. Structural Data

Bulk PbBi_2Te_4 crystallizes in a rhombohedral lattice system ($R\bar{3}m$) with seven atoms located along the c -axis (Supplementary Materials Figure S1a). However, PbBi_2Te_4 can also be treated as a hexagonal cell (Figure S1b) constituted by three seven-atom-layered slabs with three non-equivalent bonds each, held together by van de Waals interactions. One of these slabs is presented in Figure 1. It clearly shows seven atomic layers (one of Pb, two of Bi, two outmost Te layers and two inner Te ones) bonded by three non-equivalent bonds. To avoid spurious interaction between neighboring layers, the $\text{PbBi}_2\text{Te}_2\text{S}_2$, $\text{PbBi}_2\text{Te}_2\text{Se}_2$ and PbBi_2Te_4 nanosheets have been optimized with an on-top vacuum thickness of 1.6 nm. Based on our previous work on bulk Bi_2Te_3 , PbBi_2Te_4 and $\text{Pb}_2\text{Bi}_2\text{Te}_5$ [32], all of the in-layer bonds are neither pure ionic bonds nor pure covalent ones, the covalent contribution being increased when the material is subjected to compressive strains. Since both the size of the gap between slabs and the inter slabs X-X distances are also increased under compressive strains, we should expect a similar trend in the nanosheet that corresponds to an isolated slab, i.e. b_1 should be more ionic than b_2 and b_3 . If one replaces the inner Te atom by a more electronegative Se or S one, the outermost Te atom gets much less electron-rich.

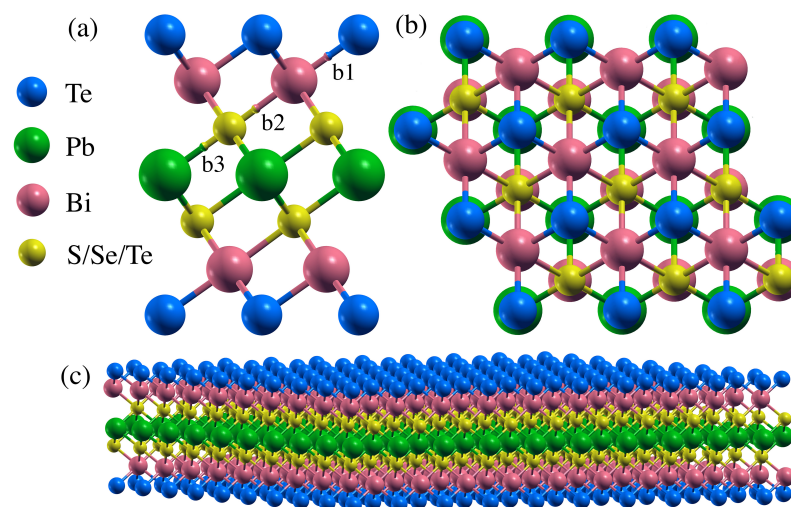


Figure 1. Side view (a), top view (b) and extended view (c) of $\text{PbBi}_2\text{Te}_2\text{X}_2$ ($X = \text{S}, \text{Se}, \text{Te}$). The three non-equivalent bonds (b_1 – b_3) are shown in (a).

The equilibrium lattice constants of $\text{PbBi}_2\text{Te}_2\text{S}_2$, $\text{PbBi}_2\text{Te}_2\text{Se}_2$ and PbBi_2Te_4 have been calculated using the WC-GGA functional [33] without spin-orbit coupling (SOC) for both bulk and nanosheet structures. The results are listed in Table 1. For bulk PbBi_2Te_4 , the optimized lattice constants are $a = 0.443$ nm, $c = 4.156$ nm and the slab thickness is 1.127 nm, which is in good agreement with reported experimental values [34]. As to the PbBi_2Te_4 nanosheet, the thickness is 1.120 nm, which is close to that of the slab in the bulk and to that reported in the literature [21]. In the septuple layers slab, each Pb atom binds with six Te atoms with identical bond length ($b_3 = 0.3210$ nm), while each Bi atom binds with six Te atoms with two sets of three identical bond lengths ($b_1 = 0.3070$ nm and $b_2 = 0.3248$ nm). If the inner Te atoms are replaced by S or Se ones, the corresponding slab thickness and bond lengths decrease.

Table 1. Calculated lattice constants, slab thickness and bond lengths as labeled in Figure 1 (b_1 is Te-Bi, b_2 is Bi-S/Se/Te and b_3 is S/Se/Te-Pb) of $\text{PbBi}_2\text{Te}_2\text{X}_2$ ($X = \text{S, Se, Te}$) in bulk and nanosheet structures optimized with the WC functional. All data in nm.

		$\text{PbBi}_2\text{Te}_2\text{S}_2$	$\text{PbBi}_2\text{Te}_2\text{Se}_2$	PbBi_2Te_4
Bulk	a	0.4230	0.4300	0.4430
	c	3.954	4.042	4.156
	Slab thickness	1.037	1.072	1.127
	b_1	0.3029	0.3051	0.3070
	b_2	0.2987	0.3085	0.3248
	b_3	0.2958	0.3046	0.3210
Nanosheet	a	0.4210	0.4280	0.4410
	c	1.041	1.074	1.128
	b_1	0.3018	0.3030	0.3048
	b_2	0.2987	0.3082	0.3244
	b_3	0.2959	0.3047	0.3203

3.2. Electronic and Transport Properties

As shown in Figure 2, $\text{PbBi}_2\text{Te}_2\text{S}_2$, $\text{PbBi}_2\text{Te}_2\text{Se}_2$ and PbBi_2Te_4 nanosheets are semiconductors with indirect energy band gaps of 0.354 eV, 0.314 eV and 0.376 eV, respectively. The band structure of PbBi_2Te_4 calculated with WC-GGA is compared in Figure S2 with that calculated with the HSE06 hybrid functional [35]. Except for the band gap, which is substantially enlarged with HSE06 (0.967 eV), both functionals qualitatively give the same results. The same observation can be done for $\text{PbBi}_2\text{Te}_2\text{Se}_2$ and $\text{PbBi}_2\text{Te}_2\text{S}_2$. Since the band gaps calculated with the WC-GGA functional are in better agreement with those reported in literature for nanosheets of homologous $\text{Pb}_m\text{Bi}_{2n}\text{Te}_{3n+m}$ compounds, which all belong to the range 0.25–0.7 eV [21], and the hybrid HSE06 functional has not been found superior to pure DFT ones in the calculations of band structures and thermoelectric properties of tetradymite materials [36], we have been using the WC-GGA functional in this work. In all the three compounds, $\text{PbBi}_2\text{Te}_2\text{S}_2$, $\text{PbBi}_2\text{Te}_2\text{Se}_2$ and PbBi_2Te_4 , the conduction band minimum (VBM) is located at the Γ point and the valence band maximum (VBM) is located along the Γ -K direction (Figure 2). In contrast to a single conduction band minimum, two, three and four valence band maxima (V_1, V_2, V_3, V_4) located within a small range of 0.1 eV wide are observed near the Fermi energy for $\text{PbBi}_2\text{Te}_2\text{S}_2$, $\text{PbBi}_2\text{Te}_2\text{Se}_2$ and PbBi_2Te_4 , respectively. In contrast to observations made in Bi_2Te_3 monolayer [8], the substitution of Se for Te in the PbBi_2Te_4 monolayer does not lead to high valence band degeneracy N_v . Compared with the conduction band, the valence band is less dispersed, leading to a higher total DOS slope and thus promising higher Seebeck coefficient for p-type material.

The analysis of partial density of states (PDOS) (see Figure S3) reveals that Te-5p, S/Se/Te-5p, Bi-6s and Pb-6s orbitals dominate the valence band near the Fermi energy, while the conduction band is dominated by Bi-6p, Pb-6p and S/Se/Te-5p orbitals. A slight contribution of the Pb-6p orbital in the valence band around the Fermi level is also evidenced. It increases for the $\text{PbBi}_2\text{Te}_2\text{X}_2$ compounds along the Te, Se and S sequence.

The bulk modulus B , elastic constants, effective mass and the cohesive energy of the compounds of interest have been calculated and the values are reported in Table 2. When X in $\text{PbBi}_2\text{Te}_2\text{X}_2$ follows the sequence Te, Se, S, the bulk modulus B increases, indicating a bond strengthening, which can be associated to the electronegativity increase of the chalcogen. One can note that, in agreement with the evolution of the band structure (Figure 2), the calculated effective mass increases with the change of inner chalcogenide layer from S to Se and Te. Indeed the top valence orbitals and bottom conduction orbitals are getting softer, leading to heavier effective mass and lower carriers mobility.

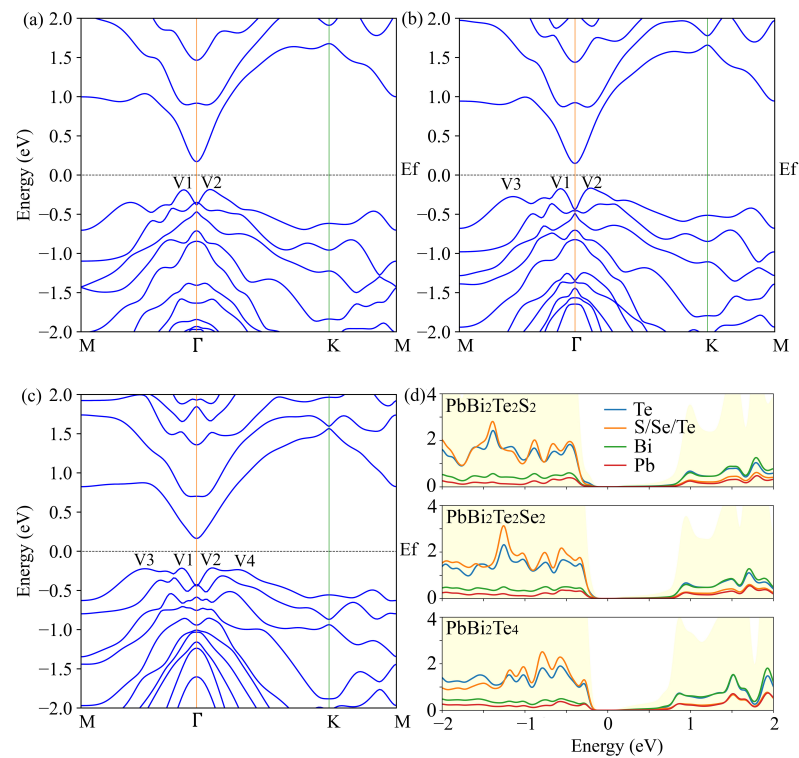


Figure 2. Electronic band structures of $\text{PbBi}_2\text{Te}_2\text{S}_2$ (a), $\text{PbBi}_2\text{Te}_2\text{Se}_2$ (b), PbBi_2Te_4 (c) and corresponding total (light yellow background) and partial (color lines) DOS (d) calculated with the WC-GGA functional and SOC.

Table 2. Bulk modulus B (GPa), bulk elastic constants C_{ij} (GPa), two-dimensional elastic constant C_{2D} (N/m), effective mass m^* (m_e) of electrons/holes, cohesive energy E_{coh} (eV/at.) at 0 K, calculated with the WC-GGA functional. (Note: The column corresponding to the deformation potential constants has been deleted).

	B	C_{11}	C_{12}	C_{13}	C_{14}	C_{33}	C_{44}	C_{2D}	m^*	E_{coh}
$\text{PbBi}_2\text{Te}_2\text{S}_2$	30.33	50.2	18.2	23.8	14.1	41.1	27.9	21.2	−0.023/0.073	−3.22
$\text{PbBi}_2\text{Te}_2\text{Se}_2$	28.75	49.5	14.5	22.7	13.5	40.2	27.0	21.2	−0.024/0.073	−3.09
PbBi_2Te_4	26.05	44.5	13.0	20.7	13.1	36.4	35.6	19.6	−0.028/0.085	−2.93

The elastic constants calculations allows for characterizing the mechanical stability of the nanosheets. The necessary and sufficient conditions of mechanical stability for the rhombohedral I system are given in Ref. [37] as

$$C_{11} > |C_{12}|; \quad C_{44} > 0$$

$$C_{13}^2 < \frac{1}{2}C_{33}(C_{11} + C_{12})$$

$$C_{14}^2 < \frac{1}{2}C_{44}(C_{11} - C_{12})$$

Our calculations show that the $\text{PbBi}_2\text{Te}_2\text{S}_2$, $\text{PbBi}_2\text{Te}_2\text{Se}_2$ and PbBi_2Te_4 monolayers are mechanically stable. Furthermore, the cohesive energies have been evaluated with the general formula: $E_{coh} = E_{tot} - \sum_i E_i$, where E_{tot} is the total energy of the monolayer, and E_i is the energy of each constitutive atom. The negative values at 0 K of the cohesive energies, namely −3.22 eV/at., −3.09 eV/at. and −2.93 eV/at. for $\text{PbBi}_2\text{Te}_2\text{S}_2$, $\text{PbBi}_2\text{Te}_2\text{Se}_2$ and PbBi_2Te_4 , respectively, also support the nanosheet stability.

Based on the above considerations, we present in Figure 3 the temperature and p-type doping dependence of the thermoelectric properties (Seebeck coefficient S , electrical

conductivity σ/τ and electronic thermal conductivity κ_e/τ) in the a-axis direction. The optimum Seebeck coefficient appears for the doping levels 10^{17} to 5×10^{19} h/cm³ and the low to intermediate 100 K–400 K temperatures, where both σ/τ and κ_e/τ are low. The largest Seebeck coefficients at room temperature are 601 $\mu\text{V}/\text{K}$, 559 $\mu\text{V}/\text{K}$, 671 $\mu\text{V}/\text{K}$ for $\text{PbBi}_2\text{Te}_2\text{S}_2$, $\text{PbBi}_2\text{Te}_2\text{Se}_2$ and PbBi_2Te_4 , respectively.

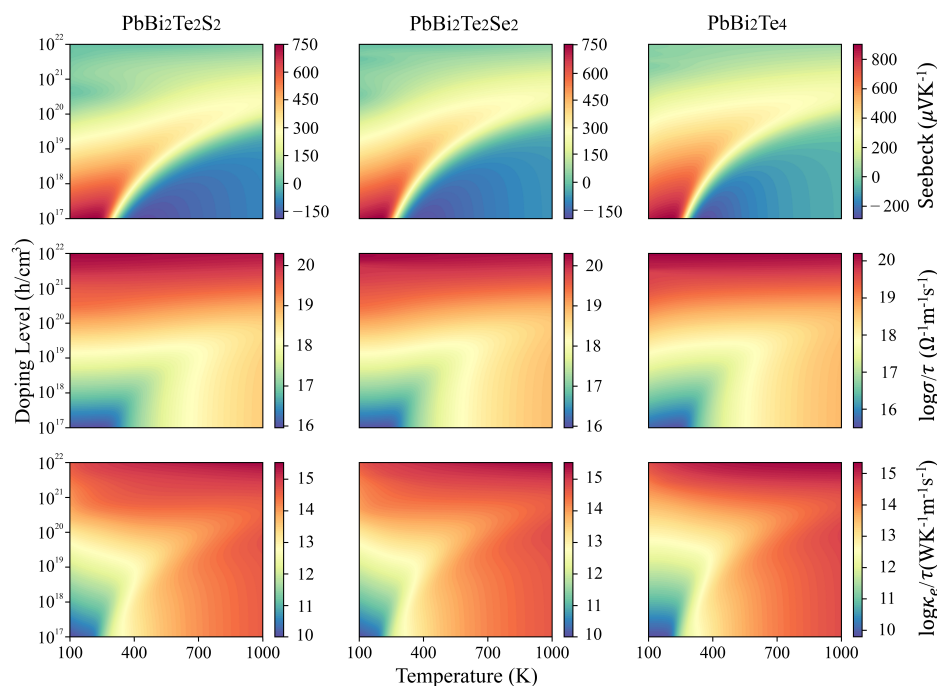


Figure 3. Calculated Seebeck coefficient and τ -scaled electrical and electronic thermal conductivities in the a-axis direction versus temperature and p-type doping levels for $\text{PbBi}_2\text{Te}_2\text{S}_2$, $\text{PbBi}_2\text{Te}_2\text{Se}_2$ and PbBi_2Te_4 .

3.3. Lattice Thermal Conductivity

The harmonic phonon spectrum depends weakly on the choice of the functional [38]. In addition, it has been reported that the LDA functionals [39] consistently give a proper bulk modulus, resulting in a better agreement with experiment for Bi_2Te_3 [40]. Hence the LDA functionals have been chosen to determine the harmonic and anharmonic IFCs. The $\text{PbBi}_2\text{Te}_2\text{S}_2$, $\text{PbBi}_2\text{Te}_2\text{Se}_2$ and PbBi_2Te_4 monolayers have been reoptimized to their relaxed states. The obtained equilibrium lattice constants are $a = 0.417$ nm, $c = 1.032$ nm for $\text{PbBi}_2\text{Te}_2\text{S}_2$, $a = 0.424$ nm, $c = 1.065$ nm for $\text{PbBi}_2\text{Te}_2\text{Se}_2$ and $a = 0.436$ nm, $c = 1.118$ nm for PbBi_2Te_4 , which are quite close to the lattice constants obtained in Section 3.1. The phonon dispersion curves together with the DOS of $\text{PbBi}_2\text{Te}_2\text{S}_2$, $\text{PbBi}_2\text{Te}_2\text{Se}_2$ and PbBi_2Te_4 are shown in Figure 4 depicting 3 acoustic and 18 optical branches. The longitudinal optical (LO)-transverse optical (TO) splitting at the Γ point is particularly large on the phonon dispersion in the m(PbTe)-n(Bi_2Te_3) system compounds [41,42], which is caused by large Born effective charges. Therefore, the contribution of the non-analytical term to the dynamical matrix has been considered and the calculated Born effective charges by the Berry phase method [43] and dielectric constants are shown in Table S1. All the monolayer crystals are dynamically stable with no imaginary modes through the whole BZ. To further ascertain the thermodynamic stability of the compounds, the Gibbs energy G has been calculated by taking into account the vibrational part of the partition function. The procedure is described in the supplemental data. Negative G values have been found for the investigated monolayers in the temperature range 0–1000 K (see Figures S4 and S5), suggesting that they are all stable. $\text{PbBi}_2\text{Te}_2\text{S}_2$ and $\text{PbBi}_2\text{Te}_2\text{Se}_2$ have similar dispersion curves with strongly interlaced optical and acoustic modes and small frequency gaps at 2.4 THz for $\text{PbBi}_2\text{Te}_2\text{Se}_2$ and 2.7 THz for $\text{PbBi}_2\text{Te}_2\text{S}_2$. For PbBi_2Te_4 , there is less crossing

between optical and acoustic branches, which will play an important role in the acoustic + acoustic \rightarrow optical scattering. Furthermore, the maximum frequencies of the acoustic phonon modes are 1.69 THz, 1.51 THz and 1.38 THz, and that of the optical phonon modes are 7.05 THz, 4.89 THz and 4.41 THz for $\text{PbBi}_2\text{Te}_2\text{Se}_2$, $\text{PbBi}_2\text{Te}_2\text{S}_2$, and PbBi_2Te_4 , respectively.

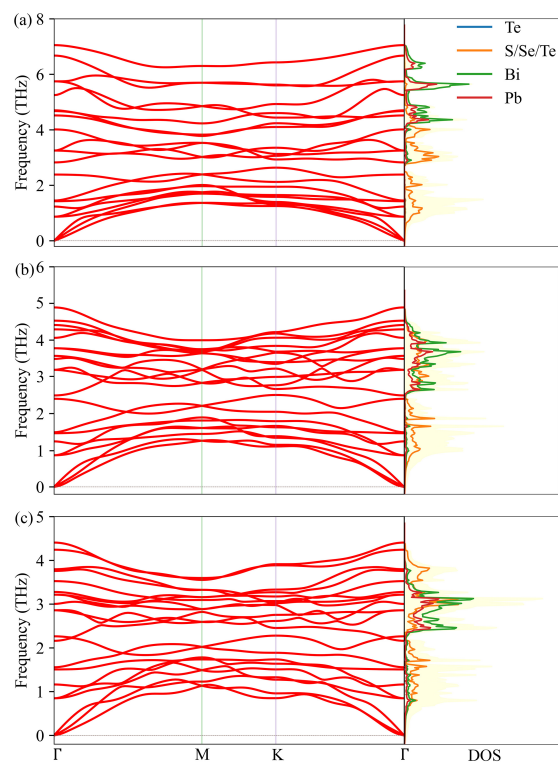


Figure 4. Phonon spectrum curves of $\text{PbBi}_2\text{Te}_2\text{S}_2$ (a), $\text{PbBi}_2\text{Te}_2\text{Se}_2$ (b), PbBi_2Te_4 (c) and corresponding total DOS (light yellow background) and projected DOS (color lines).

The lattice thermal conductivity κ_l evaluated by solving the Boltzmann transport equation (BTE) with LBTE and RTA methods is shown in Figure 5a. Contrary to RTA, the LBTE gives a rigorous way to evaluate lattice thermal conductivity by considering phonon–phonon interactions, but it necessitates huge calculations. From the LBTE method, the κ_l at room temperature of $\text{PbBi}_2\text{Te}_2\text{S}_2$, $\text{PbBi}_2\text{Te}_2\text{Se}_2$ and PbBi_2Te_4 are $0.84 \text{ W m}^{-1}\text{K}^{-1}$, $0.79 \text{ W m}^{-1}\text{K}^{-1}$ and $0.21 \text{ W m}^{-1}\text{K}^{-1}$, respectively. Although κ_l is underestimated by RTA, it is still a useful method to evaluate the phonon transport through the phonon mode group velocities and lifetimes calculations (see Figure S6). Both the average phonon lifetime and average phonon group velocity of PbBi_2Te_4 (0.64 ps and 0.32 km s^{-1}) are substantially lower than those of $\text{PbBi}_2\text{Te}_2\text{Se}_2$ (1.75 ps and 0.36 km s^{-1}) and $\text{PbBi}_2\text{Te}_2\text{S}_2$ (1.51 ps and 0.39 km s^{-1}). The detailed analysis shows that the contribution of the acoustic modes to the velocity is approximately the same in the three structures. It is noticeable that, in $\text{PbBi}_2\text{Te}_2\text{S}_2$, optical modes above 5 THz are particularly prominent with high velocity whereas they are absent in $\text{PbBi}_2\text{Te}_2\text{Se}_2$ and PbBi_2Te_4 . In addition, irrespective of the frequency domain, the phonon life time is larger for $\text{PbBi}_2\text{Te}_2\text{Se}_2$ and $\text{PbBi}_2\text{Te}_2\text{S}_2$ than for PbBi_2Te_4 . These observations explain why κ_l of PbBi_2Te_4 is lower than that of $\text{PbBi}_2\text{Te}_2\text{S}_2$ to $\text{PbBi}_2\text{Te}_2\text{Se}_2$. Slack [44] reported that intrinsically high lattice thermal conductivity can be obtained by low average atomic mass, strong interatomic bonding, simple crystal structure and strong anharmonic interaction. Since $\text{PbBi}_2\text{Te}_2\text{S}_2$, $\text{PbBi}_2\text{Te}_2\text{Se}_2$ and PbBi_2Te_4 bear roughly opposite characteristics to those just exposed, they are expected to have low lattice thermal conductivity. As mentioned above, more electronegative atoms such as Se or S compared to Te, are expected to share stronger bonding with neighbors (Pb and Bi), leading to higher lattice thermal conductivity. The trend observed in the bulk modulus of

$\text{PbBi}_2\text{Te}_2\text{S}_2$ (30.33 GPa), $\text{PbBi}_2\text{Te}_2\text{Se}_2$ (28.75 GPa) and PbBi_2Te_4 (26.05 GPa) also support the bonding strength trend and the lattice thermal conductivity one.

The τ -scaled power factor is depicted in Figure 5b,c for $\text{PbBi}_2\text{Te}_2\text{S}_2$, $\text{PbBi}_2\text{Te}_2\text{Se}_2$ and PbBi_2Te_4 as a function of the whole doping level and at temperatures 300 K, 500 K, 700 K and 900 K. The observed tendency is the same for all the compounds, namely, the maximum peak of the power factor increases with temperature, except for 300 K, where it is noticeable that the power factor of $\text{PbBi}_2\text{Te}_2\text{S}_2$ and $\text{PbBi}_2\text{Te}_2\text{Se}_2$ are about the same, whereas that of PbBi_2Te_4 is obviously lower.

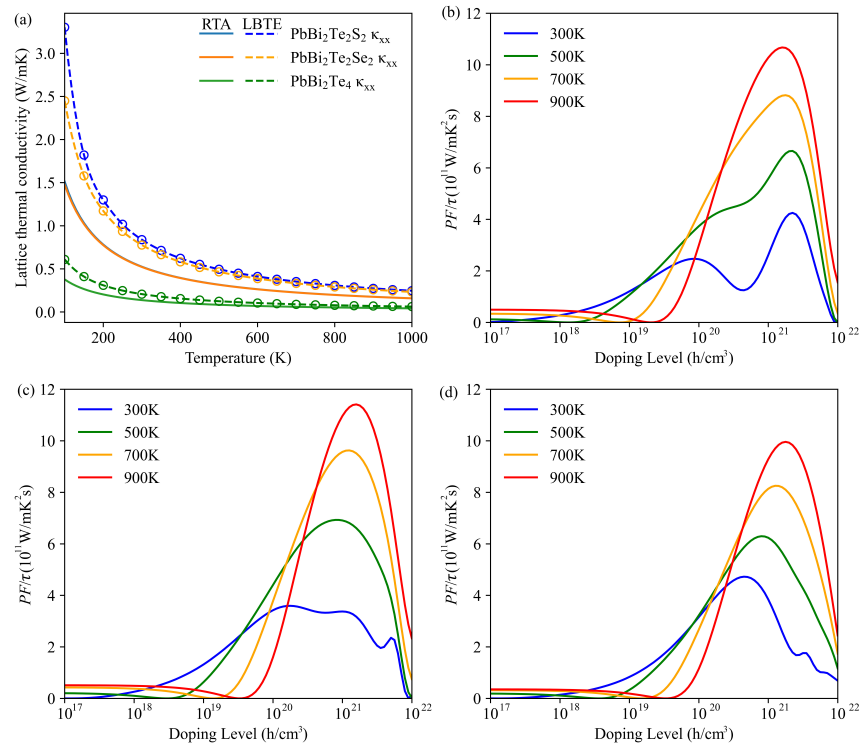


Figure 5. (a) Lattice thermal conductivity of the $\text{PbBi}_2\text{Te}_2\text{S}_2$, $\text{PbBi}_2\text{Te}_2\text{Se}_2$ and PbBi_2Te_4 as a function of temperature obtained from LBTE (dash lines) and RTA (solid lines) in the a-axis direction. Figure of merit versus hole doping level at various temperatures for $\text{PbBi}_2\text{Te}_2\text{S}_2$ (b), $\text{PbBi}_2\text{Te}_2\text{Se}_2$ (c), and PbBi_2Te_4 (d).

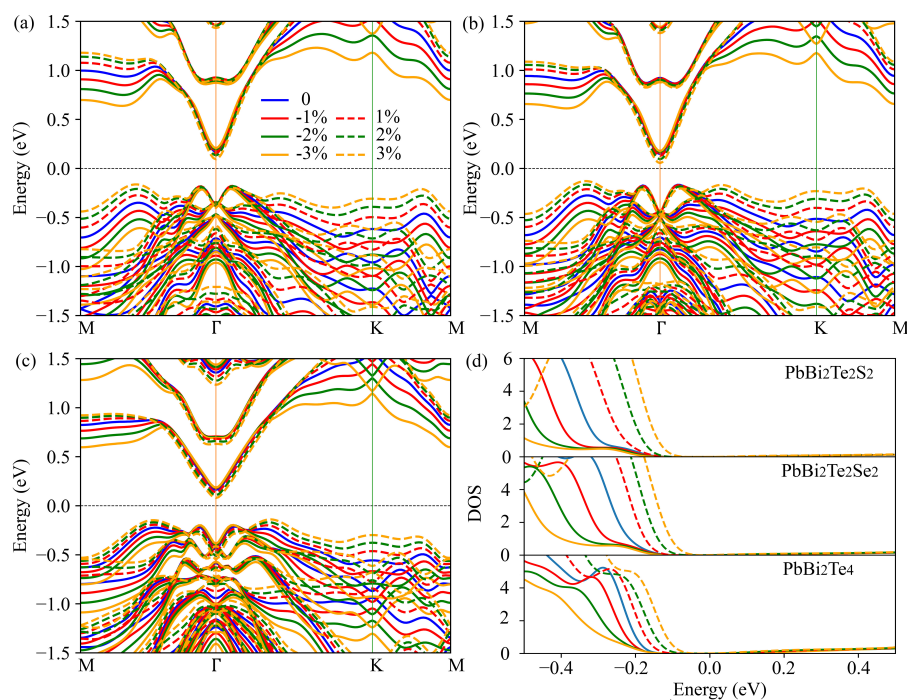
3.4. Strain Engineering of Electronic and Phonon Transport Properties

In this section we investigate the effects of in-plane biaxial strains on the electronic and phonon transport properties of the $\text{PbBi}_2\text{Te}_2\text{S}_2$, $\text{PbBi}_2\text{Te}_2\text{Se}_2$ and PbBi_2Te_4 monolayers. The positive (negative) values of strain η , which indicates the magnitude of relative tensile (compressive) strain along the a and b directions, have been calculated as $\eta = (a - a_0)/a_0$. In this work, the in-plane strains vary from -3% to 3% and the cross-plane c lattice parameter and atomic positions for each η have been optimized until the total energy and atomic forces reached their minimum. The optimized lattice parameters and total energy of the structures are listed in Table 3. The lattice constant c of the relaxed structure decreases approximately linearly under the in-plane strain changing from -3% to 3% , with a slope of 0.012 nm per unit percentage (1.15% of the lattice constant c), which shows strong coupling between a and c.

Table 3. Calculated lattice parameters a (nm), thickness c (nm), and relative energy $E_{re} = E_{\text{strained}} - E_{\text{unstrained}}$ (10^{-2} eV) of $\text{PbBi}_2\text{Te}_2\text{S}_2$, $\text{PbBi}_2\text{Te}_2\text{Se}_2$ and PbBi_2Te_4 monolayers under strains η .

Strains	$\text{PbBi}_2\text{Te}_2\text{S}_2$			$\text{PbBi}_2\text{Te}_2\text{Se}_2$			PbBi_2Te_4		
	a	c	E_{re}	a	c	E_{re}	a	c	E_{re}
−3%	4.09	10.76	8.28	4.15	11.10	10.41	4.27	11.65	9.93
−2%	4.13	10.64	3.19	4.20	10.98	4.99	4.32	11.53	4.90
−1%	4.17	10.52	0.5	4.24	10.86	1.84	4.36	11.40	1.92
0%	4.21	10.41	0	4.28	10.74	0	4.41	11.28	0
1%	4.26	10.29	0.7	4.33	10.62	1.72	4.45	11.16	1.70
2%	4.30	10.17	3.68	4.37	10.50	4.41	4.49	11.04	4.31
3%	4.34	10.05	8.74	4.41	10.38	8.90	4.54	10.91	8.52

To evidence the strain effect on the electronic structure, the bands structures and DOS of the strained and unstrained $\text{PbBi}_2\text{Te}_2\text{S}_2$, $\text{PbBi}_2\text{Te}_2\text{Se}_2$ and PbBi_2Te_4 monolayers are shown in Figure 6. The energy gap decreases slightly as the applied strain (from −3% to 3%) increases, although not leading to a semiconductor-metal transition. More interestingly, as shown in Figure 6, the valence band around Γ is very robust under strains whereas secondary valence band maxima rise in energy with the increasing tensile strains, which provides an opportunity to boost the thermoelectric properties via valence bands degeneracy. By applying strains, the derivative of the valence bands total DOS first increases and then decreases, especially for PbBi_2Te_4 . Following the band theory, the hole contribution to the Seebeck coefficient is given as [45]: $S = \frac{k_B}{e} \left[2 + \ln \left(\frac{N_V}{p} \right) \right]$, where N_V and p are the effective DOS and the number of hole carriers, respectively. Therefore, a slight tensile strain should lead to a higher Seebeck coefficient. This result is in agreement with previously reported ones. Indeed, it has been shown that slight tensile strains applied on p-type $\text{Pb}_2\text{Bi}_2\text{Te}_5$ increase the PF [32].

**Figure 6.** Electronic bands structure of $\text{PbBi}_2\text{Te}_2\text{S}_2$ (a), $\text{PbBi}_2\text{Te}_2\text{Se}_2$ (b) and PbBi_2Te_4 (c) under applied strain and their corresponding total DOS (d).

The τ -scaled PF of the $\text{PbBi}_2\text{Te}_2\text{S}_2$, $\text{PbBi}_2\text{Te}_2\text{Se}_2$ and PbBi_2Te_4 monolayers at 500 K as a function of carrier concentration are plotted in Figure 7. In all cases, the maximum PF with p-type doping increases first and then decreases with increasing applied tensile strains.

This behavior can be seen for $\text{PbBi}_2\text{Te}_2\text{S}_2$ in Figure S7, which shows the PF evolution up to 4% tensile strain.

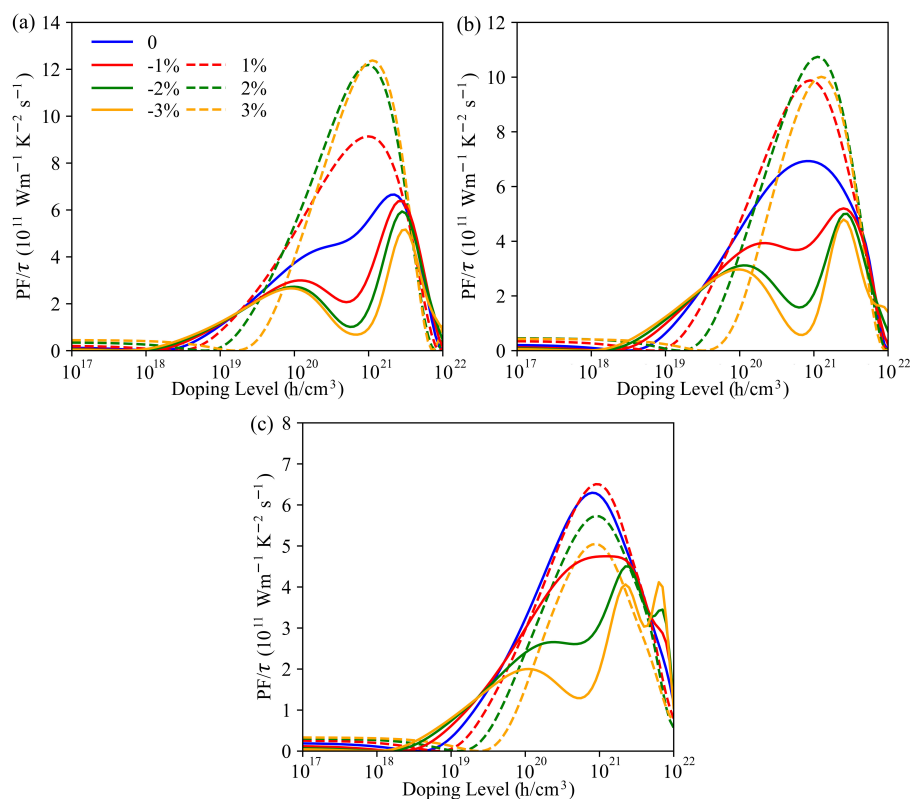


Figure 7. τ -scaled power factor of $\text{PbBi}_2\text{Te}_2\text{S}_2$ (a), $\text{PbBi}_2\text{Te}_2\text{Se}_2$ (b) and PbBi_2Te_4 (c) monolayers versus p-type doping level for various compressive and tensile strains in a-axis direction at 500 K.

The maximum PF values are found to be $12.30 \times 10^{11} \text{ Wm}^{-1}\text{K}^{-2}\text{s}^{-1}$, $10.74 \times 10^{11} \text{ Wm}^{-1}\text{K}^{-2}\text{s}^{-1}$ and $6.51 \times 10^{11} \text{ Wm}^{-1}\text{K}^{-2}\text{s}^{-1}$ for $\text{PbBi}_2\text{Te}_2\text{S}_2$, $\text{PbBi}_2\text{Te}_2\text{Se}_2$ and PbBi_2Te_4 at 3%, 2% and 1% tensile strains, respectively; they are 85.9%, 55.0% and 3.3% larger than those of unstrained structures. Therefore, it appears that an appropriate mean of optimizing the thermoelectric properties of PbBi_2Te_4 nanosheet is to substitute S/Se for Te in the inner layers and subject it to a tensile strain.

Using the same scheme as for unstrained structure, the anharmonic force constants as well as the Born effective charges and dielectric constants under strains have been calculated. The phonon spectrum curves of $\text{PbBi}_2\text{Te}_2\text{S}_2$, $\text{PbBi}_2\text{Te}_2\text{Se}_2$ and PbBi_2Te_4 along high symmetry directions are plotted in Figures 8, S8 and S9, respectively. Irrespective of the strain, no imaginary phonon modes are found in the phonon spectrum of $\text{PbBi}_2\text{Te}_2\text{S}_2$ and $\text{PbBi}_2\text{Te}_2\text{Se}_2$. By contrast, PbBi_2Te_4 shows imaginary phonon modes under -3% , -2% and 3% strains.

When strain goes from -3% to $+3\%$, the maximum frequency of the optical and acoustic phonon modes for $\text{PbBi}_2\text{Te}_2\text{S}_2$ decrease from 7.36 THz to 6.71 THz, and from 1.63 THz to 1.57 THz, respectively. According to the Slack equation [44], there is a negative correlation between κ_l and the Debye temperature, which can be defined as $\theta_i = \frac{\hbar\omega_i}{k_B}$ [46], where ω_i is the frequency of phonon mode boundary. When the strain varies from -3% to 3% , the decrease of the maximum frequency indicates a decrease of the Debye temperature, leading to more activated phonon modes, higher phonon scattering rates and hence lower lattice thermal conductivity.

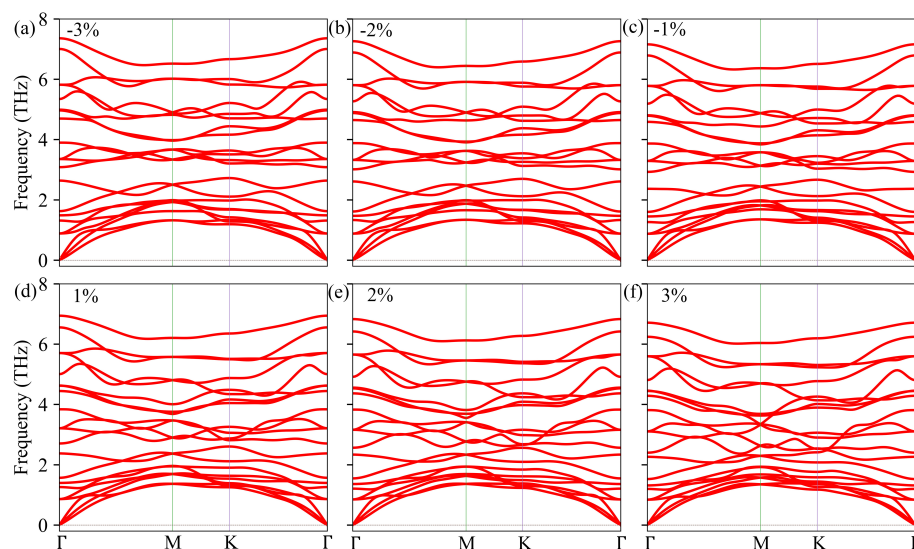


Figure 8. Phonon spectrum curves of Pb Bi₂Te₂S₂ monolayer under −3% (a), −2% (b) and −1% (c) compressive strains, and 1% (d), 2% (e) and 3% (f) tensile strains.

4. Conclusions

In summary, we have performed first-principle calculations of the electronic structure, the thermoelectric properties, the stability and the strain-engineering effects on PbBi₂Te₂S₂, PbBi₂Te₂Se₂ and PbBi₂Te₄ monolayers. All the three monolayers of interest are narrow-gap semiconductors with an indirect band gap and are energetically and thermodynamically stable without strain. In these conditions, compared with PbBi₂Te₂S₂ and PbBi₂Te₂Se₂, PbBi₂Te₄ presents a higher Seebeck coefficient, lower electrical conductivity and lower electronic thermal conductivity. The maximum Seebeck coefficient of PbBi₂Te₄ monolayer is 671 $\mu\text{V}/\text{K}$. Under small strains, the bands structures near Γ are very robust, whereas secondary valence band maxima rise in energy, leading to a valence bands alignment near the Fermi level. The highest PF/τ values are $12.38 \times 10^{11} \text{ Wm}^{-1}\text{K}^{-2}\text{s}^{-1}$, $10.74 \times 10^{11} \text{ Wm}^{-1}\text{K}^{-2}\text{s}^{-1}$ and $6.51 \times 10^{11} \text{ Wm}^{-1}\text{K}^{-2}\text{s}^{-1}$ for PbBi₂Te₂S₂, PbBi₂Te₂Se₂ and PbBi₂Te₄ at 3%, 2% and 1% tensile strains respectively. These values, which are 85.9%, 55.0% and 3.3% larger than those of the unstrained structures, prove that strain engineering is an effective approach to enhance thermoelectric properties.

Supplementary Materials: The following are available online at <https://www.mdpi.com/article/10.3390/nano11112979/nanomaterial-WMa>, Figure S1: Primitive (a) and conventional (b) cell of bulk PbBi₂Te₄. Figure S2: Calculated electronic band structures of PbBi₂Te₄ with WC-GGA (blue lines) and HSE06 hybrid (red lines) functionals. Figure S3: Calculated partial DOS of PbBi₂Te₂S₂, PbBi₂Te₂Se₂ and PbBi₂Te₄ with WC-GGA functionals. Figure S4: (a,b,c) Volume dependence of the free energy from 0 K to 900 K with a temperature step of 100K, and (d,e,f) temperature dependence of the crystal volume. PbBi₂Te₂S₂ (a,d), PbBi₂Te₂Se₂ (b,e) and PbBi₂Te₄ (c,f). Figure S5: Calculated Gibbs energy as a function of temperature for PbBi₂Te₂S₂ (a), PbBi₂Te₂Se₂ (b) and PbBi₂Te₄ (c). Figure S6: Group velocities (left panel) and phonon lifetimes (right panel) in the xx direction at 300 K for PbBi₂Te₂S₂ (top row), PbBi₂Te₂Se₂ (middle row), and PbBi₂Te₄ (bottom row). Contribution from phonon mode ZA (blue circles), TA (orange circles), LA (purple circles), optical (olive circles) branches and averaged value over a small frequency window of 0.04 THz (red lines). Figure S7: τ -scaled power factor of PbBi₂Te₂S₂ monolayer versus p-type doping level for various compressive and tensile strains in a-axis direction at 500 K. Figure S8: Phonon spectrum curves of PbBi₂Te₂Se₂ monolayer under strains. Figure S9: Phonon spectrum curves of PbBi₂Te₄ monolayer under strains. Table S1: Born effective charges Z^* (e) and dielectric constants ϵ_∞ in the in-layer and cross-layer directions [xx, zz] of PbBi₂Te₂S₂, PbBi₂Te₂Se₂ and PbBi₂Te₄ calculated with the LDA (Ceperley–Alder) functional.

Author Contributions: Conceptualization, W.M., P.B. and M.-C.R.; methodology, W.M., P.B. and M.-C.R.; software, W.M. and J.T.; formal analysis, W.M. and J.T.; writing—original draft preparation, W.M. and J.T.; writing—review and editing, P.B. and M.-C.R.; supervision, P.B. and M.-C.R.; project administration, P.B. and M.-C.R.; funding acquisition, M.-C.R. All authors have read and agreed to the published version of the manuscript.

Funding: This research received no external funding.

Institutional Review Board Statement: Not applicable.

Informed Consent Statement: Not applicable.

Data Availability Statement: See Supplementary data on MDPI website.

Acknowledgments: The authors are thankful to the China Scholarship Council for financing the PhD thesis of W. Ma and J. Tian. This work was granted access to the HPC resources of the “Centre Informatique National de l’Enseignement Supérieur (CINES)”, Montpellier, France under the allocation A0090806881 made by the “Grand Equipement National de Calcul Intensif (GENCI)”. The “Centre de Calcul Intensif d’Aix-Marseille” is acknowledged for granting access to its high performance computing resources.

Conflicts of Interest: The authors declare no conflict of interest.

References

1. Lu, X.; Zhang, Q.; Liao, J.; Chen, H.; Fan, Y.; Xing, J.; Gu, S.; Huang, J.; Ma, J.; Wang, J.; et al. High-Efficiency Thermoelectric Power Generation Enabled by Homogeneous Incorporation of MXene in $(\text{Bi,Sb})_2\text{Te}_3$ Matrix. *Adv. Energy Mater.* **2020**, *10*, 1902986. [[CrossRef](#)]
2. Liu, W.; Jie, Q.; Kim, H.S.; Ren, Z. Current Progress and Future Challenges in Thermoelectric Power Generation: From Materials to Devices. *Acta Mater.* **2015**, *87*, 357–376. [[CrossRef](#)]
3. Chowdhury, I.; Prasher, R.; Lofgreen, K.; Chrysler, G.; Narasimhan, S.; Mahajan, R.; Koester, D.; Alley, R.; Venkatasubramanian, R. On-Chip Cooling by Superlattice-Based Thin-Film Thermoelectrics. *Nat. Nanotechnol.* **2009**, *4*, 235–238. [[CrossRef](#)] [[PubMed](#)]
4. Hubbard, W.A.; Mecklenburg, M.; Lodico, J.J.; Chen, Y.; Ling, X.Y.; Patil, R.; Kessel, W.A.; Flatt, G.J.K.; Chan, H.L.; Vareski, B.; et al. Electron-Transparent Thermoelectric Coolers Demonstrated with Nanoparticle and Condensation Thermometry. *ACS Nano* **2020**, *14*, 11510–11517. [[CrossRef](#)]
5. Vining, C.B. An Inconvenient Truth about Thermoelectrics. *Nat. Mater.* **2009**, *8*, 83–85. [[CrossRef](#)] [[PubMed](#)]
6. Zhu, Q.; Song, S.; Zhu, H.; Ren, Z. Realizing High Conversion Efficiency of Mg_3Sb_2 -Based Thermoelectric Materials. *J. Power Sour.* **2019**, *414*, 393–400. [[CrossRef](#)]
7. Balout, H.; Boulet, P.; Record, M.C. Strain-Induced Electronic Band Convergence: Effect on the Seebeck Coefficient of Mg_2Si for Thermoelectric Applications. *J. Mol. Model.* **2017**, *23*, 130. [[CrossRef](#)]
8. Diznab, M.R.; Maleki, I.; Vaez Allaei, S.M.; Xia, Y.; Naghavi, S.S. Achieving an Ultrahigh Power Factor in $\text{Sb}_2\text{Te}_2\text{Se}$ Monolayers via Valence Band Convergence. *ACS Appl. Mater. Interfaces* **2019**, *11*, 46688–46695. [[CrossRef](#)]
9. Thébaud, S.; Adessi, C.; Pailhès, S.; Bouzerar, G. Boosting the Power Factor with Resonant States: A Model Study. *Phys. Rev. B* **2017**, *96*, 075201. [[CrossRef](#)]
10. Heremans, J.P.; Wiendlocha, B.; Chamoire, A.M. Resonant Levels in Bulk Thermoelectric Semiconductors. *Energy Environ. Sci.* **2012**, *5*, 5510–5530. [[CrossRef](#)]
11. Zhang, Q.; Wang, H.; Zhang, Q.; Liu, W.; Yu, B.; Wang, H.; Wang, D.; Ni, G.; Chen, G.; Ren, Z. Effect of Silicon and Sodium on Thermoelectric Properties of Thallium-Doped Lead Telluride-Based Materials. *Nano Lett.* **2012**, *12*, 2324–2330. [[CrossRef](#)]
12. Zhang, G.; Kirk, B.; Jauregui, L.A.; Yang, H.; Xu, X.; Chen, Y.P.; Wu, Y. Rational Synthesis of Ultrathin N-Type Bi_2Te_3 Nanowires with Enhanced Thermoelectric Properties. *Nano Lett.* **2012**, *12*, 56–60. [[CrossRef](#)]
13. Wu, H.J.; Zhao, L.D.; Zheng, F.S.; Wu, D.; Pei, Y.L.; Tong, X.; Kanatzidis, M.G.; He, J.Q. Broad Temperature Plateau for Thermoelectric Figure of Merit $\text{ZT} > 2$ in Phase-Separated $\text{PbTe}_{0.7}\text{S}_{0.3}$. *Nat. Commun.* **2014**, *5*, 4515. [[CrossRef](#)] [[PubMed](#)]
14. Kim, H.S.; Kim, S.I.; Lee, K.H.; Kim, S.W.; Snyder, G.J. Phonon Scattering by Dislocations at Grain Boundaries in Polycrystalline $\text{Bi}_{0.5}\text{Sb}_{1.5}\text{Te}_3$. *Phys. Status Solidi (b)* **2017**, *254*, 1600103. [[CrossRef](#)]
15. Wu, H.; Lu, X.; Wang, G.; Peng, K.; Chi, H.; Zhang, B.; Chen, Y.; Li, C.; Yan, Y.; Guo, L.; et al. Sodium-Doped Tin Sulfide Single Crystal: A Nontoxic Earth-Abundant Material with High Thermoelectric Performance. *Adv. Energy Mater.* **2018**, *8*, 1800087. [[CrossRef](#)]
16. Lu, Z.; Wu, Y.; Xu, Y.; Ma, C.; Chen, Y.; Xu, K.; Zhang, H.; Zhu, H.; Fang, Z. Ultrahigh Electron Mobility Induced by Strain Engineering in Direct Semiconductor Monolayer Bi_2TeSe_2 . *Nanoscale* **2019**, *11*, 20620–20629. [[CrossRef](#)]
17. Mishra, P.; Singh, D.; Sonvane, Y.; Ahuja, R. Two-Dimensional Boron Monochalcogenide Monolayer for Thermoelectric Material. *Sustain. Energy Fuels* **2020**, *4*, 2363–2369. [[CrossRef](#)]
18. Sun, Y.; Cheng, H.; Gao, S.; Liu, Q.; Sun, Z.; Xiao, C.; Wu, C.; Wei, S.; Xie, Y. Atomically Thick Bismuth Selenide Freestanding Single Layers Achieving Enhanced Thermoelectric Energy Harvesting. *J. Am. Chem. Soc.* **2012**, *134*, 20294–20297. [[CrossRef](#)]

19. Mounet, N.; Gibertini, M.; Schwaller, P.; Campi, D.; Merkys, A.; Marrazzo, A.; Sohler, T.; Castelli, I.E.; Cepellotti, A.; Pizzi, G.; et al. Two-Dimensional Materials from High-Throughput Computational Exfoliation of Experimentally Known Compounds. *Nat. Nanotechnol.* **2018**, *13*, 246–252. [[CrossRef](#)]
20. Ambrosi, A.; Pumera, M. Exfoliation of Layered Materials Using Electrochemistry. *Chem. Soc. Rev.* **2018**, *47*, 7213–7224. [[CrossRef](#)]
21. Chatterjee, A.; Biswas, K. Solution-Based Synthesis of Layered Intergrowth Compounds of the Homologous $Pb_mBi_{2n}Te_{3n+m}$ Series as Nanosheets. *Angew. Chem. Int. Ed.* **2015**, *54*, 5623–5627. [[CrossRef](#)]
22. Park, K.; Heremans, J.J.; Scarola, V.W.; Minic, D. Robustness of Topologically Protected Surface States in Layering of Bi_2Te_3 Thin Films. *Phys. Rev. Lett.* **2010**, *105*, 186801. [[CrossRef](#)] [[PubMed](#)]
23. Shvets, I.A.; Klimovskikh, I.I.; Aliev, Z.S.; Babanly, M.B.; Sánchez-Barriga, J.; Krivenkov, M.; Shikin, A.M.; Chulkov, E.V. Impact of Stoichiometry and Disorder on the Electronic Structure of the $PbBi_2Te_{4-x}Se_x$ Topological Insulator. *Phys. Rev. B* **2017**, *96*, 235124. [[CrossRef](#)]
24. Peng, R.; Ma, Y.; Wang, H.; Huang, B.; Dai, Y. Stacking-Dependent Topological Phase in Bilayer MBi_2Te_4 ($M = Ge, Sn, Pb$). *Phys. Rev. B* **2020**, *101*, 115427. [[CrossRef](#)]
25. Hung, N.T.; Nugraha, A.R.; Saito, R. Designing High-Performance Thermoelectrics in Two-Dimensional Tetradymites. *Nano Energy* **2019**, *58*, 743–749. [[CrossRef](#)]
26. Sharma, S.; Schwingenschlögl, U. Thermoelectric Response in Single Quintuple Layer Bi_2Te_3 . *ACS Energy Lett.* **2016**, *1*, 875–879. [[CrossRef](#)]
27. Blaha, P.; Schwarz, K.; Tran, F.; Laskowski, R.; Madsen, G.K.H.; Marks, L.D. WIEN2k: An APW+lo Program for Calculating the Properties of Solids. *J. Chem. Phys.* **2020**, *152*, 074101. [[CrossRef](#)]
28. Madsen, G.K.; Carrete, J.; Verstraete, M.J. BoltzTraP2, a Program for Interpolating Band Structures and Calculating Semi-Classical Transport Coefficients. *Comput. Phys. Commun.* **2018**, *231*, 140–145. [[CrossRef](#)]
29. Giannozzi, P.; Baroni, S.; Bonini, N.; Calandra, M.; Car, R.; Cavazzoni, C.; Ceresoli, D.; Chiarotti, G.L.; Cococcioni, M.; Dabo, I.; et al. Quantum ESPRESSO: A Modular and Open-Source Software Project for Quantum Simulations of Materials. *J. Phys. Condens. Matter* **2009**, *21*, 395502. [[CrossRef](#)]
30. Togo, A.; Chaput, L.; Tanaka, I. Distribution of Phonon Lifetime in Brillouin Zone. *Phys. Rev. B* **2015**, *91*, 094306. [[CrossRef](#)]
31. Chaput, L. Direct Solution to the Linearized Phonon Boltzmann Equation. *Phys. Rev. Lett.* **2013**, *110*, 265506. [[CrossRef](#)]
32. Ma, W.; Record, M.C.; Tian, J.; Boulet, P. Strain Effects on the Electronic and Thermoelectric Properties of $n(PbTe)-m(Bi_2Te_3)$ System Compounds. *Materials* **2021**, *14*, 4086. [[CrossRef](#)] [[PubMed](#)]
33. Wu, Z.; Cohen, R.E. A More Accurate Generalized Gradient Approximation for Solids. *Phys. Rev. B* **2006**, *73*, 235116. [[CrossRef](#)]
34. Shelimova, L.E.; Karpinskii, O.G.; Konstantinov, P.P.; Avilov, E.S.; Kretova, M.A.; Zemskov, V.S. Crystal Structures and Thermoelectric Properties of Layered Compounds in the $ATe-Bi_2Te_3$ ($A = Ge, Sn, Pb$) Systems. *Inorg. Mater.* **2004**, *40*, 451–460. [[CrossRef](#)]
35. Heyd, J.; Peralta, J.E.; Scuseria, G.E.; Martin, R.L. Energy Band Gaps and Lattice Parameters Evaluated with the Heyd-Scuseria-Ernzerhof Screened Hybrid Functional. *J. Chem. Phys.* **2005**, *123*, 174101. [[CrossRef](#)]
36. Park, S.; Ryu, B. Hybrid-Density Functional Theory Study on Band Structures of Tetradymite- Bi_2Te_3 , Sb_2Te_3 , Bi_2Se_3 , and Sb_2Se_3 Thermoelectric Materials. *J. Korean Phys. Soc.* **2016**, *69*, 1683–1687. [[CrossRef](#)]
37. Mouhat, F.; Coudert, F.X. Necessary and Sufficient Elastic Stability Conditions in Various Crystal Systems. *Phys. Rev. B* **2014**, *90*, 224104. [[CrossRef](#)]
38. Campi, D.; Paulatto, L.; Fugallo, G.; Mauri, F.; Bernasconi, M. First-Principles Calculation of Lattice Thermal Conductivity in Crystalline Phase Change Materials: $GeTe$, Sb_2Te_3 , and $Ge_2Sb_2Te_5$. *Phys. Rev. B* **2017**, *95*, 024311. [[CrossRef](#)]
39. Ceperley, D.M.; Alder, B.J. Ground State of the Electron Gas by a Stochastic Method. *Phys. Rev. Lett.* **1980**, *45*, 566.
40. Hellman, O.; Broido, D.A. Phonon Thermal Transport in Bi_2Te_3 from First Principles. *Phys. Rev. B* **2014**, *90*, 134309. [[CrossRef](#)]
41. Zhang, Y.; Ke, X.; Chen, C.; Yang, J.; Kent, P.R.C. Thermodynamic Properties of $PbTe$, $PbSe$, and PbS : A First-Principles Study. *Phys. Rev. B* **2009**, *80*, 1–12.
42. Ma, W.; Record, M.C.; Tian, J.; Boulet, P. Influence of the Stacking Sequence on Layered-Chalcogenides Properties: First Principle Investigation of $Pb_2Bi_2Te_5$. *Phys. Chem. Chem. Phys.* **2021**. [[CrossRef](#)] [[PubMed](#)]
43. King-Smith, R.; Vanderbilt, D. Theory of Polarization of Crystalline Solids. *Phys. Rev. B* **1993**, *47*, 1651. [[CrossRef](#)]
44. Slack, G.A. Nonmetallic crystals with high thermal conductivity. *J. Phys. Chem. Solids* **1973**, *34*, 321–335. [[CrossRef](#)]
45. Shalimova, K. *Fisica De Los Semiconductores*; Ergoatomizdat: Madrid, Spain, 1982.
46. Morelli, D.T.; Heremans, J.P. Thermal Conductivity of Germanium, Silicon, and Carbon Nitrides. *Appl. Phys. Lett.* **2002**, *81*, 5126–5128. [[CrossRef](#)]